Electronic Supplementary Information

MobCal-MPI 2.0: An Accurate and Parallelized Package for Calculating Field-Dependent Collision Cross Sections and Ion Mobilities

Alexander Haack[a], Christian Ieritano[a,b], W. Scott Hopkins[a,b,c]*

[a] Department of Chemistry, University of Waterloo, 200 University Ave W, Waterloo, ON, N2L 3G1, Canada.
[b] Watermine Innovation, Waterloo, Ontario, N0B 2T0, Canada.
[c] Centre for Eye and Vision Research, Hong Kong Science Park, New Territories, 999077, Hong Kong.
* Correspondence to: shopkins@uwaterloo.ca

Table of Contents

S1: Review of other CCS predictor tools

- In the mid-1990s, the MobCal program[1,2] was published for CCSs in helium, which is, arguably, the most famous CCS predictor. It allows for three different types of CCS calculations: (1) the Projection Approximation (PA), in which the "shadow" of the ion is averaged over all orientations, (2) the Exact Hard Sphere Scattering (EHSS) model, which actually calculates collision trajectories of the ion-neutral pair but treats their interaction with a hard-sphere potential, and (3) the Trajectory Method (TM), which is similar to the EHSS model but uses a more realistic Lennard-Jones (LJ) 12-6 potential. As these methods increase in accuracy (from PA to TM), their computational cost also increases. The MobCal code was later expanded to N_2 as collision gas[3,4] and further updates to the interaction potential were undertaken, specifically accounting for the polarizability of N_2 and its quadrupole moment.[5,6] Recently, further updates to the interaction potential and parallelization of the code, now termed MobCal-MPI, increased accuracy and especially speed of the calculations.[7,8]
- A lesser common known variant of the MobCal code is the HPCCS program,[9] which also utilizes the TM and can compute CCSs in He and N_2.
- The IMoS code[10–12] became also quite popular in recent years. In contrast to MobCal, IMoS explicitly calculates the drag inflicted on the ion through the bath gas. This is done by a trajectory method (with realistic interaction potentials), where the velocity of both the ion and bath gas are explicitly considered. This is in contrast to MobCal where the relative velocity of the ion-neutral pair is considered. Despite the different mathematical approach as compared to MobCal, it has been shown that both methods perform equally well.[13] IMoS then obtains the ion mobility coefficient, K, from the calculated drag and the CCS through rearranging Eq. (4) of the main manuscript.
- Collidoscope[14] is yet another CCS predicter utilizing the TM and a LJ 12-6 interaction potential including polarizability for both He and N_2 as collision gases. Its accuracy was reported to be similar to IMoS. Parallelization of the code makes it similar fast to MobCal-MPI, HPCCS and IMoS.
- Large ions (proteins, supramolecular complexes, *etc.*) make the usage of the TM both computationally infeasible but also unnecessary. Because of their size, the fine details of the scattering process become less important and projection approximation algorithms provide sufficiently accurate results. A prominent example is the PSA method.[15–18] Through careful calibration of the collision probabilities, even temperature dependencies of the CCS are reproduced.

S2: Velocity Grid Limits

In order to ensure that the integration over the relative velocity is accurate, limits for the velocity grid have to be chosen such that the integrand, $Q^{(l)}\omega^{(s)}$, is significantly close to zero at those limits. Since it is not possible to predict the magnitude and functional dependency of $Q^{(l)}(g)$, we focused on the weight functions $\omega^{(s)}$. *I.e.*, we want to find velocity limits such that upon integration, the error caused by the cutoff becomes negligible. To simplify the algebra, we work with unitless velocity and temperature:

$$g^{*2} = \frac{\mu g^2}{2\epsilon'} \tag{S1a}$$

$$T^* = \frac{k_B T}{\epsilon'} \tag{S1b}$$

Here, μ is the reduced mass of the collision pair, k_B is the Boltzmann constant, and $\epsilon' = 1.34\ \mathrm{meV}$ is a fixed energy constant (see Ref. 1). Writing the weight functions now in dimensionless units

$$\omega^{(s)}(g^*, T^*) = \left[\frac{(s+1)!}{2} T^{*s+2}\right]^{-1} \times g^{*2s+3} \exp\left(-\frac{g^{*2}}{T^*}\right) \tag{S2}$$

we can express their integrals as:

$$\int_0^{G_{upper}} \omega^{(s)}(g^*, T^*)\, \mathrm{d}g^* = 1 - \frac{1}{(s+1)!}\, \Gamma\left(s+2, \frac{G_{upper}^2}{T^*}\right) \tag{S3a}$$

$$\int_{G_{lower}}^{\infty} \omega^{(s)}(g^*, T^*)\, \mathrm{d}g^* = \frac{1}{(s+1)!}\, \Gamma\left(s+2, \frac{G_{lower}^2}{T^*}\right) \tag{S3b}$$

where Γ is the upper incomplete gamma function and G_{lower} and G_{upper} define the lower and upper limit for the velocity integration, respectively. From this, we can obtain and G_{lower} and G_{upper} by defining acceptable errors, *i.e.*, asking how close the integrals of Eq. (S3) should be to unity:

$$\frac{1}{(s+1)!}\, \Gamma\left(s+2, \frac{G_{upper}^2}{T^*}\right) = \xi_{upper} \tag{S4a}$$

$$\frac{1}{(s+1)!}\, \Gamma\left(s+2, \frac{G_{lower}^2}{T^*}\right) = 1 - \xi_{lower} \tag{S4b}$$

Because $Q^{(l)}(G_{lower}) \gg Q^{(l)}(G_{upper})$, we pick a tighter value for ξ_{lower}. However, a too low G_{lower} will result in lost trajectories because at very low relative velocities collision particles will stick to/orbit the ion. In the end, we picked:

$$\xi_{upper} = 10^{-3} \overset{s=4}{\rightleftarrows} G_{upper} = \sqrt{16.455 \cdot T_{upper}^*} \tag{S5a}$$

$$\xi_{lower} = 10^{-4} \overset{s=1}{\rightleftarrows} G_{lower} = \sqrt{0.0862 \cdot T_{lower}^*} \tag{S5b}$$

Here, T_{lower}^* is calculated from T_{bath} and T_{upper}^* is calculated from $T_{eff,max}$ according to Eq. (S1b).

S3: Collision Dynamics

The amount of momentum transferred upon a collision between two particles (at relative velocity g, impact parameter b and assuming a spherically symmetric interaction potential), can be calculated from the scattering angle, χ, and is proportional to $1 - \cos\chi$. In Figure S1, some example trajectories are shown for two different relative velocities and a set of impact parameters (ranging from $b = 0$ to a cut-off value b_{max}). It further shows the amount of momentum being transferred as a function of the impact parameter. The integral under these curves is proportional to the momentum transfer cross section, $Q^{(1)}(g)$. We can separate collision events into two categories: glancing collisions (large b, only probing the attractive part of the potential) and striking collisions (small b, probing both the attractive and repulsive part of the potential). Both kinds contribute to the overall momentum transfer for small velocities but as can be seen in Figure S1, for higher relative velocities, only the striking collisions transfer momentum. In particular, at higher velocities trajectories with large b do not significantly contribute to the total momentum transfer.

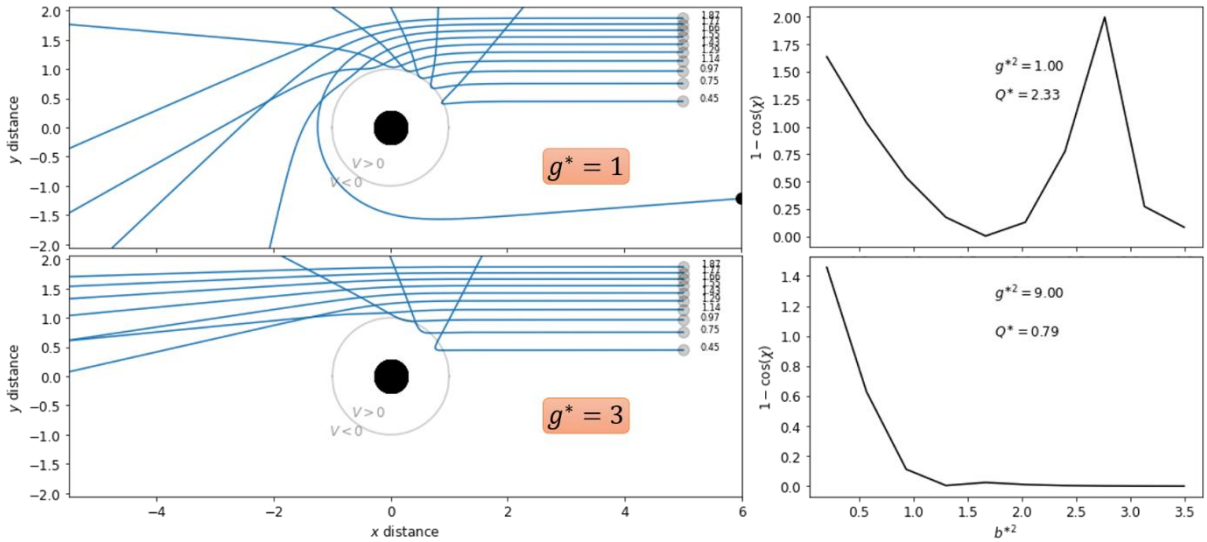

Figure S1: Left: Collision trajectories for two different relative speeds, g^*, and for a set of impact parameters, b^* (in dimensionless units). Right: Corresponding momentum transfer as a function of b^{*2}. The interaction potential is assumed to be spherically symmetric and the grey circle denotes the distance at which the potential becomes repulsive.

Thus, when integrating over both the velocity as well as impact parameter space, using a common upper limit, b_{max}, will result in a lot of trajectories that do not contribute to the overall momentum transfer integrals. This can be seen even better in Figure S2, which shows the momentum transfer as contour plot over both velocity and impact parameter space. As can be seen, most trajectories (started at pairs of (b, g)) would yield close to zero momentum transfer and can thus be neglected to save computing time. Consequently, it is beneficial to calculate a b_{max} value for each velocity grid point. This was already done in the original MobCal implementation and we keep this strategy here. This is depicted with the red line in Figure S2. This way, at every of the *inp* velocity points, *imp* impact parameter (and orientation) samples are taken, but only for $b \leq b_{max}(g)$, where there is significant momentum transfer.

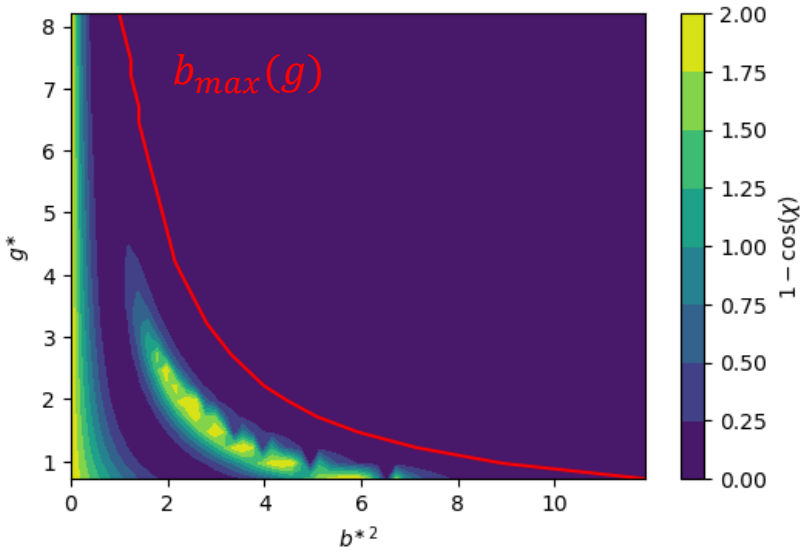

Figure S2: Left: Contour plot of $1-\cos\chi$ (proportional to the momentum transfer) as a function of the impact parameter, b, and the relative velocity, g, of the colliding particles (both in dimensionless units). The red line denotes the threshold values $b_{max}(g)$ for every velocity point.

S4: Avg-N2 versus CoM-N2 Potentials

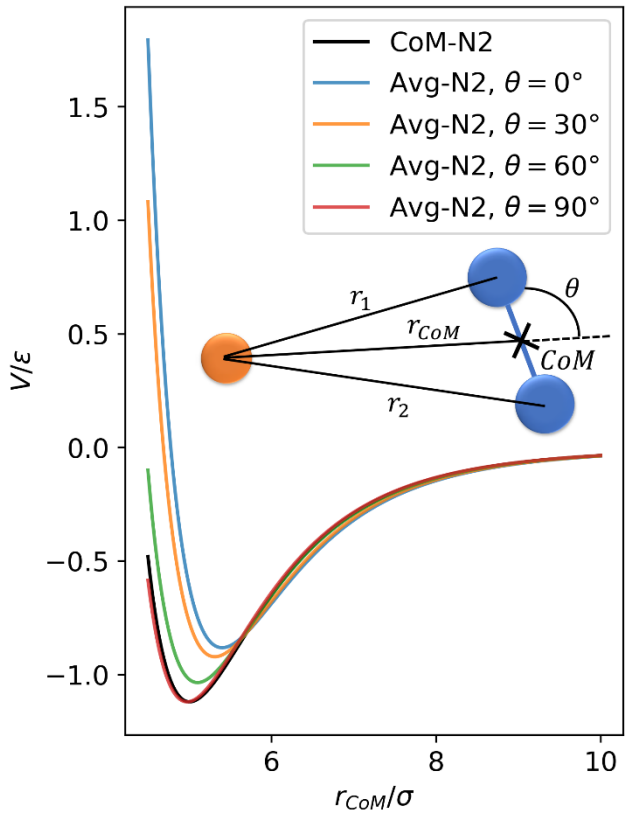

Figure S3: Van-der-Waals interaction potentials (Exp-6) for the CoM-N_2 and Avg-N_2 versions depending on the orientation of the N_2 molecule (described by the angle θ). While the CoM-N_2 potential is independent on θ, the Avg-N_2 potential shows a strong dependency. Importantly, for a head-on collision ($\theta = 0°$), the potential becomes repulsive faster. This is more realistic because for a head-on collision, one end of the N_2 molecule reaches the collision partner significantly earlier than its CoM.

S5: Precision for high-field calculations

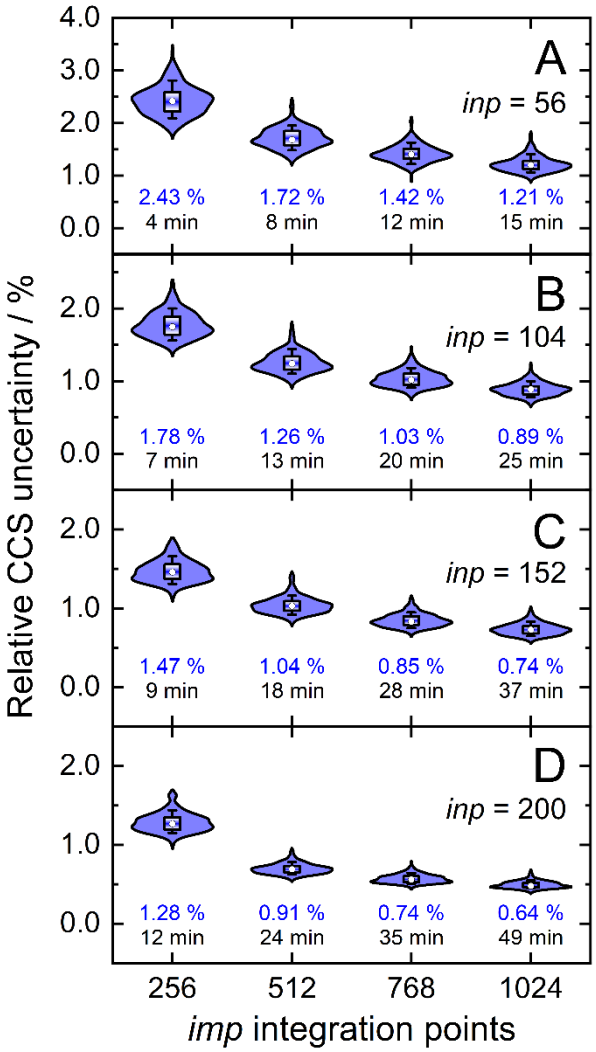

Figure S4: Distributions of relative CCS uncertainties, $\sigma_{CI}\left(\Omega^{(1,1)}\right)/\Omega^{(1,1)}$, for the validation set (N=50) for different combinations of velocity sample points (inp) and orientation/impact parameter sample points (imp) when calculating mobilities/CCS between 298 K and 800 K. Blue numbers below each distribution correspond to mean relative CCS uncertainties and black numbers to average computing time.

S6: Empirical Correction

S6.1: Choice of functional form

Siems *et al.*[19] compared 2nd order 2TT with accurate modelling of an ion's mobility using the Gram-Charlier (GC) approach for idealized test systems, *i.e.*, atomic ions in atomic gases. They found that 2TT yields good results over a broad range of field strength (0-50 Td), but shows 5-7% deviations above 100 Td. In particular, for the "heavy ion" case, *i.e.*, when the ion is much heavier than the bath gas particle, the deviations are zero at low fields, then the 2TT mobilities become increasingly too small, eventually reaching a constant underestimation at very high field strengths. In order to correct for this deviation, we should pick a form that matches this behavior: no deviations at low fields, constant deviation at very high fields and a smooth transition in between. We chose

$$K_{corr} = f_{corr} \cdot K_{2TT} \tag{S6a}$$

$$f_{corr}\left(\frac{E}{N}\right) = 1 + A \exp\left(-\frac{B}{E/N}\right) \tag{S6b}$$

and as can be seen in Figure S5, the form of f_{corr} fulfills these requirements. At low fields $f_{corr} = 1$ so that $K_{corr} = K_{2TT}$. Increasing the field strength leads to an increase in f_{corr} up to a fixed correction of $K_{corr} = (1 + A)K_{2TT}$ in the limit of very high E/N, corresponding to a relative increase of the mobility by A (%). How fast we switch from $f_{corr} = 1$ to $f_{corr} = 1 + A$ is determined by B.

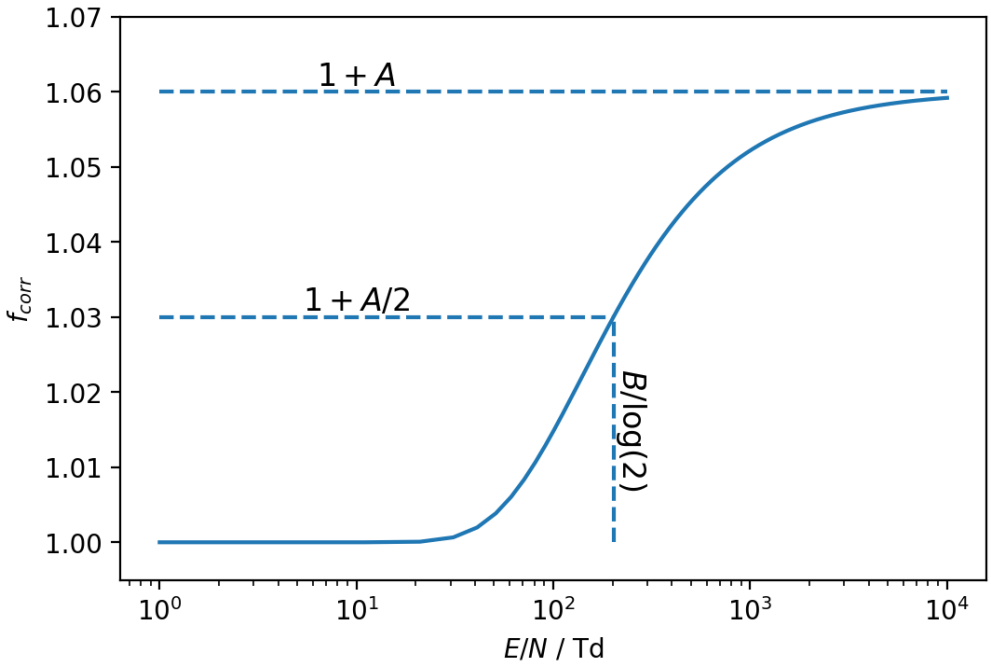

Figure S5: Functional form of the empirical correction used here. The parameters A and B determine the limit at very high fields and the speed of the rise, respectively. Here, we used exemplary values of $A = 6\ \%$ *and* $B = 140$ Td.

A rough estimate of the magnitude of A and B that we expect for the situations studied here can be obtained when comparing Figure S5 with the deviations shown by Siems *et al*. This way, we obtain $A \approx 7\%$ and $B \approx 120$ Td.

Further justification of the functional form chosen comes from comparison of the difference between measured and predicted alpha function of protonated amoxapine (see Fig. 6A of the main manuscript). Given multiplicative nature of our correction (Eq. (S6a)), we can obtain the needed correction from the experimental and 2TT predicted alpha function according to

$$f_{true} = \frac{\alpha_{expt}+1}{\alpha_{2TT}+1} \tag{S7}$$

Comparing this function to the form of f_{corr} from Eq. (S6b) using the fitted parameters, A and B, shows large overlap, as can be seen in Figure S6. It is interesting to note that the field strengths used in the DMS (from which α_{expt} was obtained through the formalism described in Section S7) are not large enough for the correction function to reach its asymptote, $1 + A$.

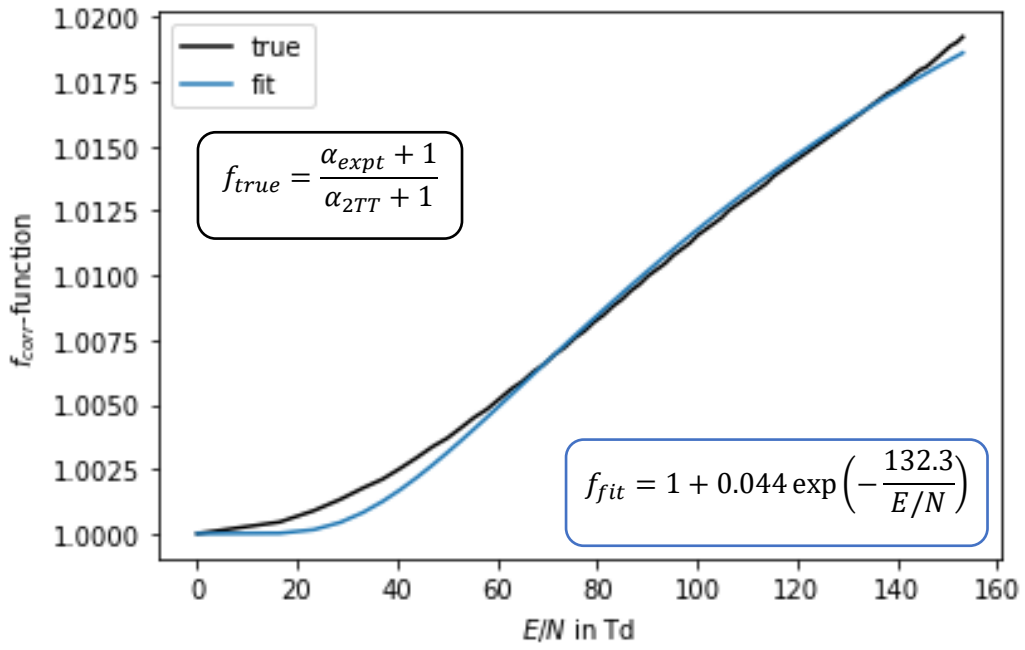

Figure S6: Comparison of the real deviations between experimental and 2TT calculated alpha function (black line, "true") and the empirical correction function used here, applying the optimal parameters $A = 4.4$ % and $B = 132.3$ Td.

S6.2: Examples of dispersion plots utilizing the empirical correction

Calculated mobilities within 2nd order 2TT (K_{2TT}) were used to model dispersion plot behavior of the 132 compounds in the "high-field validation set" according to the method (see Section S7). In general, we find that 2TT overestimated the measured dispersion plots, which is in line with the deviations found by Siems *et al*. To study to what extend K_{2TT} needs to be corrected, we fitted the parameters A and B for all 132 compounds, such that the experimental dispersion plots were predicted most efficiently. As explained in the main manuscript, the average over all parameters A and B were then used as common empirical correction.

The results of this procedure can be seen in Figure S7 for two examples. As was mentioned, it can be seen that the uncorrected 2TT overshoots the measured dispersion plots. Individual fitting of the empirical correction, however, yields dispersion plots that are very well within the experimental uncertainties. This gives us confidence that the functional form chosen is well suited for this task. Finally, Figure S7 shows the calculated dispersion plots utilizing the fixed empirical correction (A_{avg}, B_{avg}). In case of Bentazon, this still yields very good agreement with the experimental data since the individually fitted empirical correction parameters are almost identical to the averaged ones. In contrast, the fixed empirical correction shows larger deviations to the experimental data as compared

to the individually fitted ones. This can also be seen by comparing the correction parameters, which are rather different for the individually and fixed empirical correction. Specifically, the fixed empirical correction if too large and thus corrects the mobilities more than needed. Nevertheless, we would argue that the dispersion plot with (fixed) empirical correction resembles the experimental one better or at least as good at the uncorrected 2TT predicted one. Salicylic acid belongs to one of the more difficult cases, in general we find much better agreement (see main manuscript).

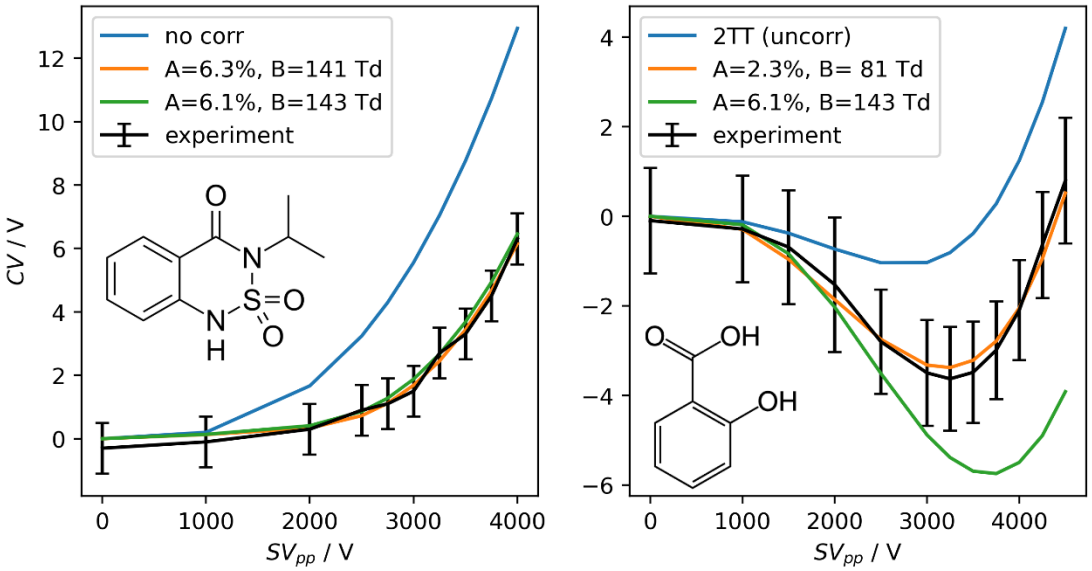

Figure S7: Measured and calculated dispersion plots of Bentazon (left) and Salicylic Acid (right). Calculated dispersion plots are shown for uncorrected 2nd order 2TT, for 2TT with individually fitted empirical correction, and for 2TT with the fixed empirical correction utilizing $A_{avg} = 6.1\%$ and $B_{avg} = 143\ Td$.

S6.3: Correlation of A and B parameters

Before resorting to using the average of the distributions of A and B, i.e., A_{avg} and B_{avg}, we tried correlating the optimized values to typical properties appearing in the formulation of collision dynamics. However, as can be seen in Figure S8, we do not find any significant correlation to any of the studies quantities.

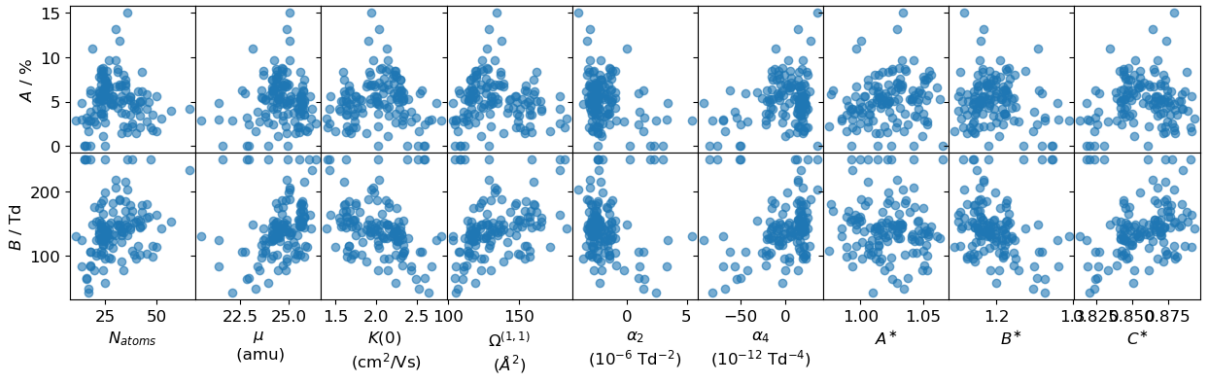

Figure S8: Correlation between the A and B parameters to typical parameters appearing in the formalism of ion mobility, namely the number of atoms (N_{atoms}), the reduced mass (μ), the low field mobility (K(0)), the first collision integral ($\Omega^{(1,1)}$), alpha function coefficients (α_2 and α_4) and important ratios of collision integrals ($A^* = \Omega^{(2,2)}/\Omega^{(1,1)}$, $B^* = (5\Omega^{(1,2)} - 4\Omega^{(1,3)})/\Omega^{(1,1)}$, and $C^* = \Omega^{(1,2)}/\Omega^{(1,1)}$).

S7: Connection between alpha function and dispersion plot

The alpha function of an ion describes how the mobility at higher field strengths deviates from its value at infinitely small field strengths:

$$\alpha\left(\frac{E}{N}\right) = \frac{K\left(\frac{E}{N}\right)}{K(0)} - 1 \tag{S8}$$

In differential mobility spectrometry, to probe this alpha function, an asymmetric, oscillating field is applied containing both high- and low-field strengths. This separation field, $E_S(t)$ can have many forms (square wave, double sine, etc.)[20] but it is required that

$$\frac{1}{\tau}\int_0^\tau E_S(t)\,\mathrm{d}t = \langle E_S(t)\rangle = E_S\langle f(t)\rangle = 0 \tag{S9a}$$

$$\langle f^{2n+1}(t)\rangle \neq 0 \tag{S9b}$$

where $E_S(t) = E_S f(t)$ with $f(t)$ being the normalized form of the waveform and E_S its amplitude (maximum value). τ denotes the time for one wave cycle. Additional to the separation field, a constant field, E_C, is applied to ensure ion transmission. Thus, the total field is

$$E(t) = E_S f(t) + E_C \tag{S10}$$

A dispersion plot now measures the compensation field, E_C, ideal for ion transmission in dependence of the separation field amplitude, E_S.

To obtain the alpha function from a measured dispersion plot, Buryakov[21] suggested the following method: First, the dispersion plot data is fitted to an uneven polynomial of $(2N+1)$-th order:

$$E_C = \sum_{n=1}^{N} B_{2n+1} E_S^{2n+1} \tag{S11}$$

The obtained coefficients B_{2n+1} can then be used to determine the alpha function, expressed as even polynomial:[21,22]

$$\alpha(E) = \sum_{n=1}^{N} \alpha_{2n} E^{2n} \tag{S12a}$$

$$\alpha_{2n} = \frac{1}{\langle f^{2n+1}(t)\rangle}\left\{B_{2n+1} + \sum_{k=1}^{n-1}(2(n-k)+1)B_{2k+1}\alpha_{2(n-k)}\langle f^{2(n-k)}\rangle\right\} \tag{S12b}$$

Note that this workflow can show deviations at the higher end of the field strengths, as is the case with every polynomial fitting. The lower end ($E \to 0$) is not an issue since the enforcement of $B_0 = \alpha_0 = 0$ ensures the correct behaviour, namely $E_C(E_S = 0) = 0$ and $\alpha(E = 0) = 0$.

Conversely, the dispersion plot can also be predicted from knowing the alpha function. If E_C is expected to be very small as compared to E_S, Buryakov's first order approximation equation can be used:[21]

$$E_C = \frac{\langle \alpha f(t)\rangle E_S}{1 + \langle\alpha\rangle + \langle \alpha' f(t)\rangle E_S} \tag{S13}$$

Note, that $\alpha = \alpha\big(E_S(t)\big)$ but we omitted the field dependency for notational clarity. Further, $\alpha' = \mathrm{d}\alpha/\mathrm{d}E$.

However, this equation breaks down if E_C becomes large as we recently showed in another publication.[23] In this case, the compensation value, E_C, can be determined iteratively. *I.e.*, starting with a guess, $E_C^{(guess)}$, we calculate the net drift velocity of the ion caused by the asymmetry of the waveform according to

$$\langle v_D\rangle = \langle K \cdot [E_S f(t) + E_C^{(guess)}]\rangle \tag{S14}$$

Again, note that we omitted the explicit dependency of the mobility on the total separation field, $K = K\big(E(t)\big) = K(E_S f(t) + E_C)$. The mobility can be obtained from the alpha function by rearranging Eq. (S8). We then use the obtained net drift velocity to obtain a new guess for the separation field as

$$E_C^{(new)} = E_C^{(old)} - \frac{\langle v_D \rangle}{K(0)} \delta_{damp} \tag{15}$$

where δ_{damp} is a damping factor usually used in iterative procedures. The new guess of E_C is used again in Eq. (S14) and this procedure is repeated until $\langle v_D \rangle < v_{thresh}$, *i.e.*, until the drift velocity left is negligible.

S8: Benchmarking

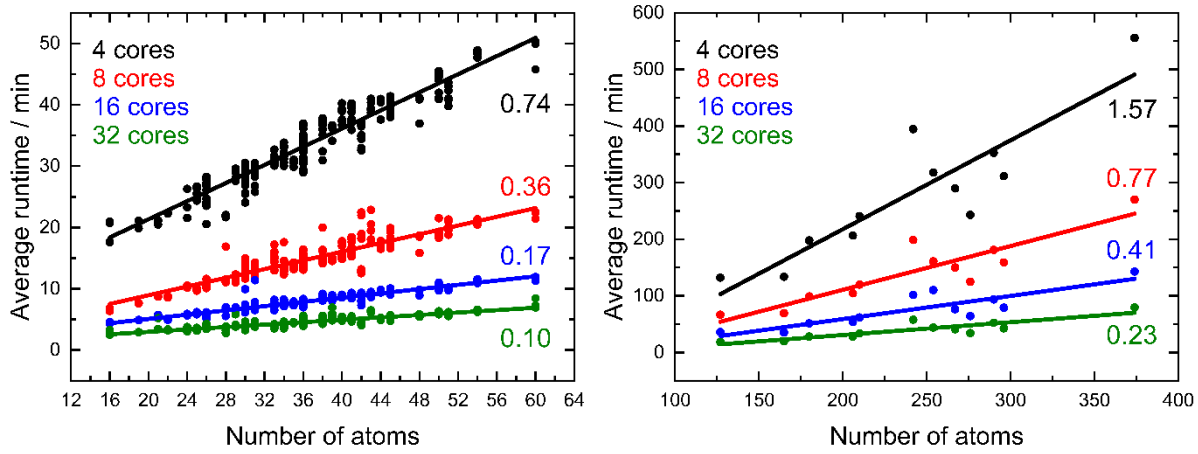

Figure S9: Benchmarking of runtimes to calculate CCSs in dependence of the number of cores used in parallel computing. ***Left****: Test data is composed of the 238 different conformers of the validation set.* ***Right****: Test data is composed of 12 peptides from the peptide set. All calculations are repeated for three different random seed numbers. The linear behavior shows the expected $O(N)$ dependency with respect to the number of atoms, whereas the 1/N_{cores} decrease in the slopes (numbers adjacent to the regressions) shows the good performance of the parallelization.*

References

(1) Mesleh, M. F.; Hunter, J. M.; Shvartsburg, A. A.; Schatz, G. C.; Jarrold, M. F. Structural Information from Ion Mobility Measurements: Effects of the Long-Range Potential. *J. Phys. Chem.* **1996**, *100* (40), 16082–16086. https://doi.org/10.1021/jp961623v.

(2) Shvartsburg, A. A.; Jarrold, M. F. An Exact Hard-Spheres Scattering Model for the Mobilities of Polyatomic Ions. *Chem. Phys. Lett.* **1996**, *261* (1–2), 86–91. https://doi.org/10.1016/0009-2614(96)00941-4.

(3) Kim, H.; Kim, H. I.; Johnson, P. V.; Beegle, L. W.; Beauchamp, J. L.; Goddard, W. A.; Kanik, I. Experimental and Theoretical Investigation into the Correlation between Mass and Ion Mobility for Choline and Other Ammonium Cations in N 2. *Anal. Chem.* **2008**, *80* (6), 1928–1936. https://doi.org/10.1021/ac701888e.

(4) Campuzano, I.; Bush, M. F.; Robinson, C. V.; Beaumont, C.; Richardson, K.; Kim, H.; Kim, H. I. Structural Characterization of Drug-like Compounds by Ion Mobility Mass Spectrometry: Comparison of Theoretical and Experimentally Derived Nitrogen Collision Cross Sections. *Anal. Chem.* **2012**, *84* (2), 1026–1033. https://doi.org/10.1021/ac202625t.

(5) Lee, J. W.; Davidson, K. L.; Bush, M. F.; Kim, H. I. Collision Cross Sections and Ion Structures: Development of a General Calculation Method via High-Quality Ion Mobility Measurements and Theoretical Modeling. *Analyst* **2017**, *142* (22), 4289–4298. https://doi.org/10.1039/C7AN01276D.

(6) Lee, J. W.; Lee, H. H. L.; Davidson, K. L.; Bush, M. F.; Kim, H. I. Structural Characterization of Small Molecular Ions by Ion Mobility Mass Spectrometry in Nitrogen Drift Gas: Improving the Accuracy of Trajectory Method Calculations. *Analyst* **2018**, *143* (8), 1786–1796. https://doi.org/10.1039/C8AN00270C.

(7) Ieritano, C.; Crouse, J.; Campbell, J. L.; Hopkins, W. S. A Parallelized Molecular Collision Cross Section Package with Optimized Accuracy and Efficiency. *Analyst* **2019**, *144* (5), 1660–1670. https://doi.org/10.1039/C8AN02150C.

(8) Ieritano, C.; Hopkins, W. S. Assessing Collision Cross Section Calculations Using MobCal-MPI with a Variety of Commonly Used Computational Methods. *Mater. Today Commun.* **2021**, *27* (February), 102226. https://doi.org/10.1016/j.mtcomm.2021.102226.

(9) Zanotto, L.; Heerdt, G.; Souza, P. C. T.; Araujo, G.; Skaf, M. S. High Performance Collision Cross Section Calculation-HPCCS. *J. Comput. Chem.* **2018**, *39* (21), 1675–1681. https://doi.org/10.1002/jcc.25199.

(10) Larriba, C.; Hogan, C. J. Free Molecular Collision Cross Section Calculation Methods for Nanoparticles and Complex Ions with Energy Accommodation. *J. Comput. Phys.* **2013**, *251*, 344–363. https://doi.org/10.1016/j.jcp.2013.05.038.

(11) Larriba, C.; Hogan, C. J. Ion Mobilities in Diatomic Gases: Measurement versus Prediction with Non-Specular Scattering Models. *J. Phys. Chem. A* **2013**, *117* (19), 3887–3901. https://doi.org/10.1021/jp312432z.

(12) Larriba-Andaluz, C.; Fernández-García, J.; Ewing, M. A.; Hogan, C. J.; Clemmer, D. E. Gas Molecule Scattering & Ion Mobility Measurements for Organic Macro-Ions in He versus N 2 Environments. *Phys. Chem. Chem. Phys.* **2015**, *17* (22), 15019–15029. https://doi.org/10.1039/C5CP01017A.

(13) Shrivastav, V.; Nahin, M.; Hogan, C. J.; Larriba-Andaluz, C. Benchmark Comparison for a Multi-Processing Ion Mobility Calculator in the Free Molecular Regime. *J. Am. Soc. Mass Spectrom.* **2017**, *28* (8), 1540–1551. https://doi.org/10.1007/s13361-017-1661-8.

(14) Ewing, S. A.; Donor, M. T.; Wilson, J. W.; Prell, J. S. Collidoscope: An Improved Tool for Computing Collisional Cross-Sections with the Trajectory Method. *J. Am. Soc. Mass Spectrom.* **2017**, *28* (4), 587–596. https://doi.org/10.1007/s13361-017-1594-2.

(15) Bleiholder, C.; Wyttenbach, T.; Bowers, M. T. A Novel Projection Approximation Algorithm for the Fast and Accurate Computation of Molecular Collision Cross Sections (I). Method. *Int. J. Mass Spectrom.* **2011**, *308* (1), 1–10. https://doi.org/10.1016/j.ijms.2011.06.014.

(16) Bleiholder, C.; Contreras, S.; Do, T. D.; Bowers, M. T. A Novel Projection Approximation Algorithm for the Fast and Accurate Computation of Molecular Collision Cross Sections (II). Model Parameterization and Definition of Empirical Shape Factors for Proteins. *Int. J. Mass Spectrom.* **2013**, *345–347*, 89–96. https://doi.org/10.1016/j.ijms.2012.08.027.

(17) Anderson, S. E.; Bleiholder, C.; Brocker, E. R.; Stang, P. J.; Bowers, M. T. A Novel Projection Approximation Algorithm for the Fast and Accurate Computation of Molecular Collision Cross Sections (III): Application to Supramolecular Coordination-Driven Assemblies with Complex Shapes. *Int. J. Mass Spectrom.* **2012**, *330–332*, 78–84. https://doi.org/10.1016/j.ijms.2012.08.024.

(18) Bleiholder, C.; Contreras, S.; Bowers, M. T. A Novel Projection Approximation Algorithm for the Fast and Accurate Computation of Molecular Collision Cross Sections (IV). Application to Polypeptides. *Int. J. Mass Spectrom.* **2013**, *354–355*, 275–280. https://doi.org/10.1016/j.ijms.2013.06.011.

(19) Siems, W. F.; Viehland, L. A.; Hill, H. H. Correcting the Fundamental Ion Mobility Equation for Field Effects. *Analyst* **2016**, *141* (23), 6396–6407. https://doi.org/10.1039/C6AN01353H.

(20) Krylov, E. V; Coy, S. L.; Vandermey, J.; Schneider, B. B.; Covey, T. R.; Nazarov, E. G. Selection and Generation of Waveforms for Differential Mobility Spectrometry. *Rev. Sci. Instrum.* **2010**, *81* (2), 024101. https://doi.org/10.1063/1.3284507.

(21) Buryakov, I. A.; Krylov, E. V.; Nazarov, E. G.; Rasulev, U. K. A New Method of Separation of Multi-Atomic Ions by Mobility at Atmospheric Pressure Using a High-Frequency Amplitude-Asymmetric Strong Electric Field. *Int. J. Mass Spectrom. Ion Process.* **1993**, *128* (3), 143–148. https://doi.org/10.1016/0168-1176(93)87062-W.

(22) Krylov, E.; Nazarov, E. G.; Miller, R. A.; Tadjikov, B.; Eiceman, G. A. Field Dependence of Mobilities for Gas-Phase-Protonated Monomers and Proton-Bound Dimers of Ketones by Planar Field Asymmetric Waveform Ion Mobility Spectrometer (PFAIMS). *J. Phys. Chem. A* **2002**, *106* (22), 5437–5444. https://doi.org/10.1021/jp020009i.

(23) Haack, A.; Hopkins, W. S. Kinetics in DMS: Modeling Clustering and Declustering Reactions. *J. Am. Soc. Mass Spectrom.* **2022**, *33* (12), 2250–2262. https://doi.org/10.1021/jasms.2c00224.